COMMUNICATION

Control of Double-Vortex Domain Configurations in a Shape-Engineered Trilayer Nanomagnet System

By *Lei Huang, Marvin A. Schofield,* and *Yimei Zhu**

Intense interest in nanomagnetic materials is stimulated by the continuing quest for smaller, faster, and more energy efficient magnetic devices.[1,2] Rapid miniaturization has pushed the physical dimensions of magnetic devices into the submicrometer region, where new and intriguing size-dependent phenomena take effect.[3–5] At this length scale, the exchange and magnetostatic energies are of comparable magnitude and small variations of size or shape in the nanomagnetic system dramatically alters the energy levels and ground-state spin configuration. Moreover, to achieve specific functionality, especially with multicomponent devices, the overall magnetization process must be precisely engineered to ensure reliable operation.[6,7] Accordingly, the ability to effectively probe and analyze complex multilayer spin configurations and magnetization processes plays a key role in the development of next-generation magnetic nanotechnologies.[8]

Here, we focus on a novel nanometric trilayer structure consisting of two shape-engineered permalloy (Py, $Ni_{80}Fe_{20}$) layers separated by a nonmagnetic aluminum (Al) spacer, as a model experimental system. Using electron holography techniques, as described in the Experimental section, we directly characterize the magnetization reversal behavior of individual trilayer stacks and show that separate chirality-controlled vortex nucleation and annihilation events in the two magnetic layers are responsible for the underlying reversal mechanism. Accordingly, we exploit this reversal behavior to systematically obtain four distinct configurations of flux-closure, double-vortex states at remanence that are controllably generated by applying defined magnetic-field sequences to individual nanomagnetic trilayer stacks.

The flux-closure state is attractive in device application to minimize undesired interaction between neighboring nanomagnets.[9] Specifically, the magnetic vortex state is characterized by a planar curling of the magnetic spin configuration with a specific chirality (either clockwise (CW) or counter-clockwise (CCW)) around a nanometer-sized vortex region, wherein the magnetization achieves an out-of-plane spin polarity.[10] The magnetic vortex state is acquired (through nucleation) in the ground-state remanent configuration, for nanomagnets within a certain range of aspect ratios for the characteristic planar dimension and thickness.[11] Here, we combine a semi-square and semi-disk planar shape to control the vortex chirality upon nucleation as illustrated by micromagnetic simulations for a single-layer structure (Fig. 1).

Figure 1 shows the schematic image of a nanomagnet used for simulation purposes, with a characteristic planar dimension of 400 nm × 400 nm and a thickness of 20 nm. The element is initially saturated parallel to the straight edge, either along the positive *x*-direction (top row) or the negative *x*-direction (bottom row). When the field is reduced from saturation, the magnetic spin curls along the straight edge of the element to minimize stray-field generation. Due to the asymmetric shape, the overall magnetization adopts the so-called ''C-state'' configuration with the strongest curling region located close to the straight edge. This region serves as the vortex nucleation site once the field is further reduced. Importantly, the chirality of nucleated vortex is directly determined by the initial orientation of the applied field as shown in the simulations.

Previous studies indicate that magnetic layers of different thickness, but with the same planar dimensions, switch at different stages during a hysteresis cycle since the critical fields for vortex nucleation and expulsion are strongly dependent on the geometric aspect ratio of lateral size and thickness.[11] Hence, a trilayer stack, consisting of two magnetic layers of different thickness separated by a non-magnetic spacer, shows different switching behavior in the individual magnetic layers. Moreover, along with the chirality-control mechanism, these well-separated critical switching fields enable the development of protocols for the application of the magnetic field in order to generate remanent double-vortex states with specific chirality combinations across the multilayer structure.

Experimentally, we prepared 400-nm-wide trilayer semi-square/semi-disk shaped elements, as detailed in the Experimental section. A schematic of the trilayer architecture is shown in the inset of Figure 2. Experiments were conducted on dozens of individual elements and Figure 2 shows typical experimental measurements performed during one hysteresis cycle, where the field was applied parallel to the straight edge of the particular element. The perimeter of Figure 2 shows cosine maps of the 4× amplified electron-optical phase shift recovered from electron holograms recorded at various points of applied field and can be directly interpreted as the projected induction. The density of fringes is the magnitude of the induction, where one period of fringe corresponds to ¼ of an enclosed flux quantum of 2.07×10^3 T nm^2. The interior of Figure 2 shows the net

[*] Prof. Y. Zhu, L. Huang, Dr. M. A. Schofield
Condensed Matter Physics and Material Science Department
Brookhaven National Laboratory
Upton, NY 11973 (USA)
E-mail: zhu@bnl.gov
Prof. Y. Zhu, L. Huang
Department of Physics and Astronomy
Stony Brook University
Stony Brook, NY 11794-3800 (USA)

DOI: 10.1002/adma.200902488

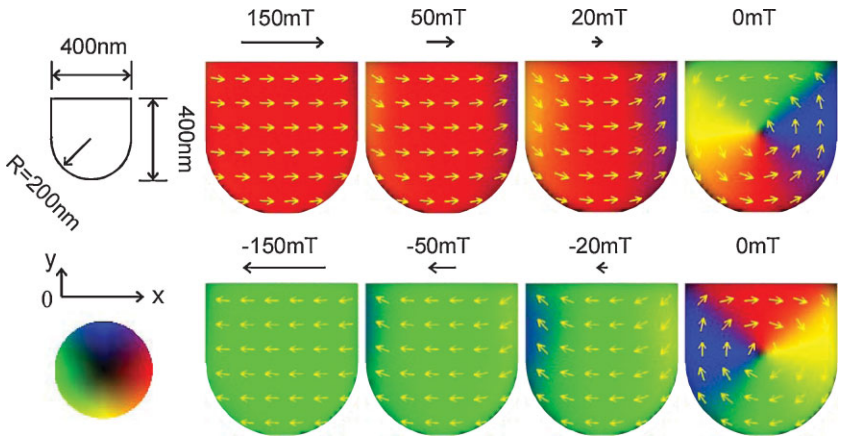

Figure 1. Chirality-controlled vortex nucleation process of a single-layer shape-engineered magnetic element. The simulated sample was a 400-nm-wide, 20-nm-thick Py element shown schematically on the top left. Simulations were performed with a LLG micromagnetic simulator on a discrete $128 \times 128 \times 1$ grid, where a magnetic field is applied along the horizontal *x*-direction. Top row: The element is initially saturated (150 mT) in the $+x$ direction. After relaxation, a CCW vortex is nucleated. Bottom row: The element is initially saturated in the $-x$ direction. After relaxation, a CW vortex is nucleated.

induction of the element as a function of applied field, with a one-to-one correspondence between the data points on the loop and a real-space visualization of the local magnetic structure of the element through its entire thickness. This is a unique advantage of electron holography techniques and is unparalleled in gaining a comprehensive understanding of the magnetic reversal processes of individual nanoscale magnetic elements as opposed to volume-averaged techniques, such as superconducting quantum interference devices (SQUID) magnetometry involving hundreds or thousands of individual elements.[12]

Starting from saturation at 149 mT (Figure 2, top right), the induction within the sample area is essentially uniform. Outside the element, the stray field closely resembles that of a magnetic dipole. As the field is reduced to 43 mT, both magnetic layers evolve into C-states as evidenced by the curling of the induction map. At 24 mT, a CCW vortex (V1) is nucleated in the 10-nm Py layer, while the 20-nm Py layer remains in the C-state. The nucleation of V1 leads to the formation of a closed flux loop within the sample region, which is clearly visible in the contours of the 21 mT induction map. This nucleation event triggers a sudden decrease of the net magnetization, which is reflected as a jump in the hysteresis loop at the arrow position labeled N10. At 12 mT, a CCW vortex (V2) is nucleated in the 20-nm Py layer. We attribute the nucleation of V1 to the 10-nm layer and the nucleation of V2 to the 20-nm layer by comparing the relative magnitudes of the two associated jumps in the hysteresis loop. Below 12 mT the induction contours outside the sample area are virtually absent, indicating a flux-closure state and a strongly suppressed stray field. When the field is decreased to zero and then increased in the reverse direction, both V1 and V2 propagate toward the curved edge of the sample geometry. Vortex V1 is expelled at around –22 mT, followed by V2 at around −40 mT. These two expulsion events also contribute to two jumps in the hysteresis loop, as indicated in Figure 2. The sample subsequently adopts the C-state configuration and, finally, a uniformly aligned saturation state upon further increase of the reversed field. The other branch of the hysteresis loop is similarly analyzed and a double-CW-vortex configuration is formed at remanence.

We performed micromagnetic simulations on the same structure; details are provided in Supporting Information. The underlying reversal mechanism, involving separate chirality-controlled vortex nucleation and annihilation events (i.e., two nucleation and two expulsion events) in the two magnetic layers, were well reproduced. The critical field values for the expulsion events agree with our experiment, however, the nucleation values differ significantly. This is because the idealized simulation does not

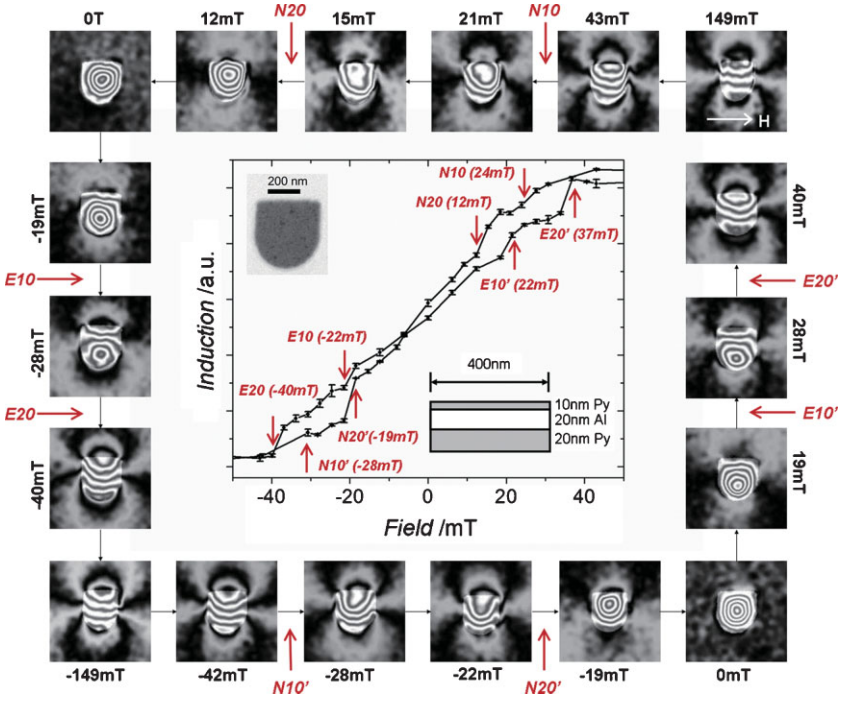

Figure 2. Experimentally measured hysteresis loop with corresponding induction contours at representative field stages. Each point of the hysteresis loop is an average of phase maps obtained from three holograms; the error bar shows the standard deviation of the measurement. Red arrows mark the vortex nucleation fields (N) and expulsion fields (E) in each layer of thickness, 10 nm and 20 nm (labeled 10 and 20, respectively), at the specified measured field values. The top-left inset in the graph shows the bright-field TEM image of the sample. The bottom-right inset shows a schematic representation of the sample geometry. Perimeter: induction contour images generated by performing the cosine operation on the 4× amplified magnetic phase shift. Note that the element region is slightly highlighted for visual guidance.

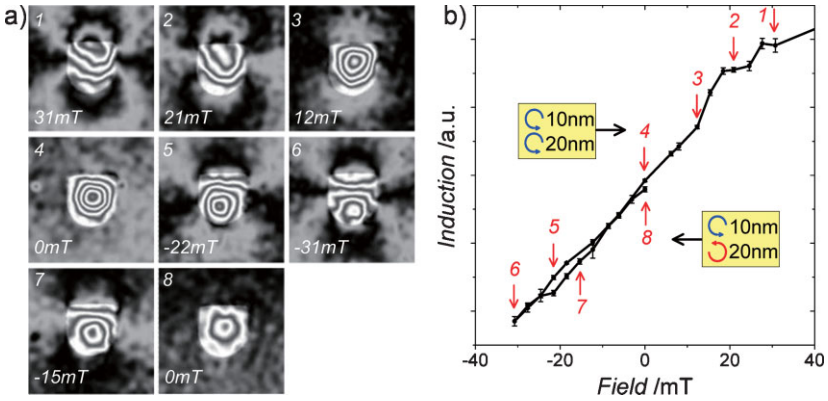

Figure 3. Detailed process of generating a double-vortex remanent state with a chirality configuration CW/CCW in the 10 nm/20 nm Py layers. a) 4× amplified induction maps obtained from electron holograms recorded at specified values of applied field. b) Hysteresis loop of the measured induction versus applied field. The protocol for the magnetic field application is a minor loop derived from the full hysteresis curve shown in Figure 2.

include structural imperfections of a real sample, such as grain boundaries or edge roughness, that can substantially delay the vortex nucleation process within individual layers.[13,14] In this regard, advanced electron microscopy techniques provide essential information to directly bridge the structure–property relationship of individual elements and to test the validity of the theory.

From the detailed reversal behavior, shown in Figure 2, we developed a protocol for the magnetic field application to manipulate remanent double-vortex states with specific chirality combinations. There are four remanent states, each consisting of two centered vortices with chirality combinations of CW/CW, CW/CCW, CCW/CCW, and CCW/CW for the 10 nm/20 nm Py layers. In Figure 2, we already demonstrated the recipes to generate the two remanent states with the same relative vortex chirality, CW/CW and CCW/CCW, by saturating the trilayer structure in the appropriate direction along the straight edge, and then relaxing it to remanence. The CW/CW and CCW/CCW configurations correspond to the lower-right and upper-left induction maps in Figure 2. To generate the other two states with opposite relative chirality combinations, the sample is first saturated and then brought through a minor hysteresis loop to achieve the desired remanent state. As a concrete example, we detail the generation of the CW/CCW state in Figure 3, where first the CCW/CCW state is created as described above. The field is then increased in the reverse direction, stopping between the two expulsion fields associated with each vortex, V1 and V2. At this point, the 10-nm layer, with an expelled vortex, is in the C-state, while the 20-nm layer still preserves the vortex. By relaxing the field back to remanence, a CW vortex is nucleated in the 10-nm layer leading to the formation of a CW/CCW (10 nm/20 nm) double-vortex arrangement.

All four field protocols and the corresponding remanent states are summarized in Figure 4, which includes line-scan comparisons between the measured and calculated phase shift for each remanent-state spin configuration. After applying specific field sequences, as outlined in Figure 4, each double-vortex domain configurations was obtained by micromagnetic simulation. The resultant spin-vector distributions of two magnetic layers were then utilized to numerically calculate the projected electron phase shift, using the Fourier-transform based method developed by Beleggia and Zhu.[15] The measured values agree well with the calculations in both the distribution profile and the peak amplitude. More importantly, this directly confirms the feasibility of using defined field sequences to generate specific double-vortex states in a fully controllable manner. The concept and functionality of this artificial structure

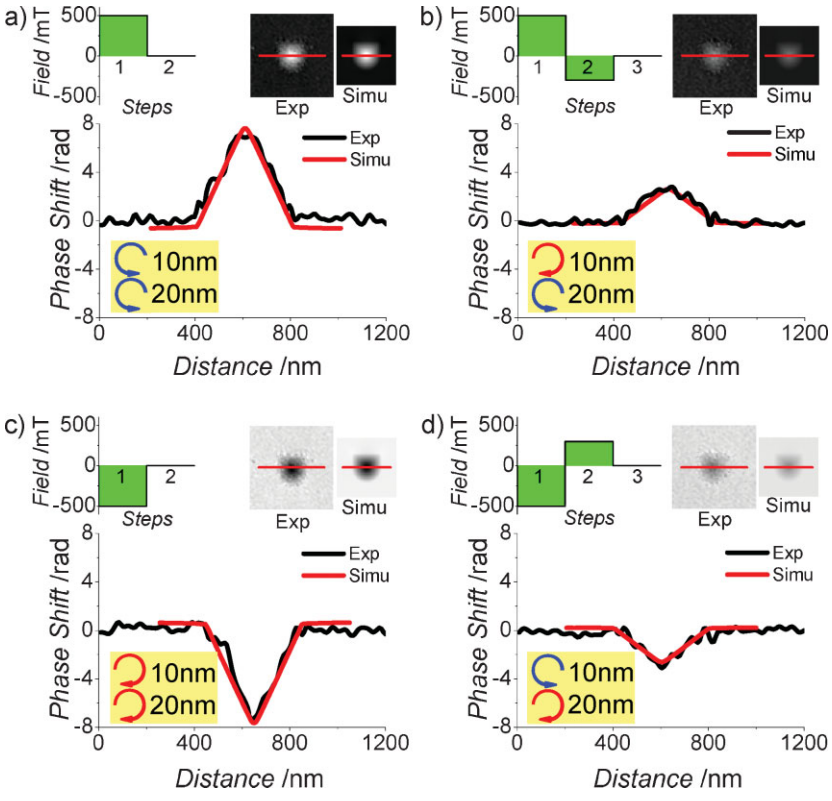

Figure 4. Controlling the remanent vortex chirality configurations by applied field. The yellow boxed inset shows the chirality configuration from the applied field sequence (green plots) to obtain the remanent state. a) Remanent CCW/CCW state in the 10 nm/20 nm Py layers. Comparison of the measured and simulated phase profiles (inset phase maps) are plotted in black-dotted and red-solid lines, respectively. The additional panels (b–d) correspond to the remaining three remanent chirality configurations CW/CCW, CW/CW, and CCW/CW, respectively.

can therefore be incorporated into the future design of quaternary memory architectures, as opposed to the conventional binary systems of "on/off" bits.[16]

To summarize, using advanced nanolithography methods, we have fabricated a unique trilayer structure that generates four stable and distinct magnetic configurations at remanence. We showed the detailed and quantitative layer-resolved physical processes of magnetization-reversal behavior, using the electron holography methods we developed, and demonstrated how remanent magnetic configurations are obtained and controlled in this model system by systematic manipulation of the applied field. Our work clearly demonstrates the feasibility of designing and fabricating shape-engineered structures for well-controlled, high-density recording devices via vortex states that have virtually no remanent stray field generated between the closely packed data bits.

Experimental

Sample Preparation: Samples were fabricated on 50-nm-thick amorphous Si_3N_4 supporting membranes for transmission electron microscopy (TEM) experiments. Standard procedures of electron-beam lithography, using bilayer poly(methyl methacrylate) (PMMA) resist, and electron-beam deposition and lift-off were carried out successively to prepare the patterned elements. During the deposition step, a 3-nm-thick Ti seed layer was used to enhance the surface adhesion to the Si_3N_4 substrate and a 3-nm-thick Al capping layer was added to prevent oxidation. After lift-off, the whole specimen surface was coated with 1-nm C to reduce specimen charging during TEM observations. All materials used were deposited at a base pressure lower than 5×10^{-5} Pa and at evaporation rates of less than 0.1 nm s^{-1}.

Off-axis Electron Holography: Off-axis electron holography experiments, were carried out using a 300 kV JEM-3000F electron microscope. In situ magnetization was performed by tilting the sample in the magnetic field of the objective lens [17]. Specifically, the objective-lens excitation was fixed at 0.25 V, generating a 353 mT field along the optic axis, i.e., perpendicular to the sample. The tilt of the sample stage was varied between $+25^\circ$ and -25° to change the in-plane component of the field between +149 mT and −149 mT, which was approximated to represent the applied magnetic field. Due to the high aspect ratio of the thin film structure and a strong demagnetization effect, the perpendicular field component has only a slight influence on the reversal process [18]. Samples used in this study were routinely checked in our field-free electron microscope (JEM2100F-LM) to assure that in situ magnetization experiments conducted on the JEM-3000F instrument were not adversely affected, in particular their remanent-state spin configuration, by the residual perpendicular component of the applied field.

Acknowledgements

The authors gratefully acknowledge M. Beleggia, V. V. Volkov, and J. W. Lau for stimulating discussions. Sample preparation was carried out at the Center for Functional Nanomaterials, Brookhaven National Laboratory. This work is supported by the U.S. Department of Energy, Office of Basic Energy Science, under Contract number DE-AC02-98CH10886. Supporting Information is available online from Wiley InterScience or from the author.

Received: July 21, 2009
Published online: October 20, 2009

[1] C. Chappert, A. Fert, F. N. Van Dau, *Nat. Mater.* **2007**, *6*, 813.
[2] I. Zutic, J. Fabian, S. Das Sarma, *Rev. Mod. Phys.* **2004**, *76*, 323.
[3] S. D. Bader, *Rev. Mod. Phys.* **2006**, *78*, 1.
[4] C. L. Chien, F. Q. Zhu, J. G. Zhu, *Phys. Today* **2007**, *60*, 40.
[5] T. Kasama, R. E. Dunin-Borkowski, M. R. Scheinfein, S. L. Tripp, J. Liu, A. Wei, *Adv. Mater.* **2008**, *20*, 4248.
[6] S. A. Wolf, D. D. Awschalom, R. A. Buhrman, J. M. Daughton, S. von Molnar, M. L. Roukes, A. Y. Chtchelkanova, D. M. Treger, *Science* **2001**, *294*, 1488.
[7] D. D. Awschalom, M. E. Flatte, *Nat. Phys.* **2007**, *3*, 153.
[8] M. R. Freeman, B. C. Choi, *Science* **2001**, *294*, 1484.
[9] F. Q. Zhu, D. L. Fan, X. C. Zhu, J. G. Zhu, R. C. Cammarata, C. L. Chien, *Adv. Mater.* **2004**, *16*, 2155.
[10] T. Shinjo, T. Okuno, R. Hassdorf, K. Shigeto, T. Ono, *Science* **2000**, *289*, 930.
[11] K. Y. Guslienko, V. Novosad, Y. Otani, H. Shima, K. Fukamichi, *Phys. Rev. B* **2002**, *65*, 024411.
[12] M. Heumann, T. Uhlig, J. Zweck, *Phys. Rev. Lett.* **2005**, *94*, 077202.
[13] J. W. Lau, R. D. McMichael, S. H. Chung, J. O. Rantschler, V. Parekh, D. Litvinov, *Appl. Phys. Lett.* **2008**, *92*, 012506.
[14] J. W. Lau, R. D. McMichael, M. A. Schofield, Y. Zhu, *J. Appl. Phys.* **2007**, *102*, 023916.
[15] M. Beleggia, M. A. Schofield, Y. Zhu, M. Malac, Z. Liu, M. Freeman, *Appl. Phys. Lett.* **2003**, *83*, 1435.
[16] B. F. Soares, F. Jonsson, N. I. Zheludev, *Phys. Rev. Lett.* **2007**, *98*, 4.
[17] R. E. Dunin-Borkowski, M. R. McCartney, D. J. Smith, S. S. P. Parkin, *Ultramicroscopy* **1998**, *74*, 61.
[18] M. Schneider, H. Hoffmann, J. Zweck, *Appl. Phys. Lett.* **2000**, *77*, 2909.